INTERNATIONAL JOURNAL FOR NUMERICAL METHODS IN FLUIDS
Int. J. Numer. Meth. Fluids 2004; **45**:985–1008 (DOI: 10.1002/fld.735)

Cubic eddy-viscosity turbulence models for strongly swirling confined flows with variable density

Xiaodong Yang[‡,§] and Huiyang Ma[*,†]

Graduate School of the Chinese Academy of Sciences, Beijing, People's Republic of China

SUMMARY

An investigation on the predictive performance of cubic eddy-viscosity turbulence models for strongly swirling confined flows with variable density is presented. Comparisons of the prediction with the experiments show some improvements of cubic models over the linear k–ε model. The linear k–ε model does not contain any mechanism to represent the interaction of swirl and density variation and as a consequence it performs poorly. With appropriate modelling, two-equation cubic turbulence models can capture the subcritical nature of the flow, represent the azimuthal velocity profiles of combined forced-free vortex motion, and predict the combined effects of swirl and density variation fairly well. However, the calibration of model coefficients is still a topic of investigation. Further amendments are also needed for the equations of k and ε to take into account the effects of swirl and density gradients correctly.

KEY WORDS: strongly swirling flow; confined flow; variable density; turbulence modelling; cubic eddy-viscosity models

1. INTRODUCTION

Swirling flows are widely used in industrial applications, such as combustion chambers and furnaces. At sufficient degree of swirl, a recirculation region is created at the axis of symmetry to enhance mixing of the fuel and oxidant, anchor the flame and achieve complete combustion in the shortest possible distance. In particular, strongly swirling confined flows examined experimentally by So *et al.* [1] and Escudier *et al.* [2] tend to display undesirable features, having a near-stagnant or weakly recirculation region at the axis of symmetry. These flows are close to subcritical and are highly sensitive to downstream perturbations, essentially due to the decay of the production rates of the shear stresses affected by the rotational strain [3]. In the experiments of So *et al.* [1], Ahmed and So [4], So and Ahmed [5], the variable density

*Correspondence to: Huiyang Ma, Graduate School of the Chinese Academy of Sciences, Beijing, People's Republic of China.
†E-mail: hyma@163bj.com
‡Graduate student.
§E-mail: xy2103@columbia.edu

Published online 4 May 2004
Received 21 June 2003
Revised 7 March 2004

effects on jet mixing in strongly swirling confined flows is investigated. It is shown that the decay of jet and mixing between jet fluid and surrounding air are influenced by the interaction between swirl, density variation and turbulence. In the case of the air jet, the central jet will be in equilibrium. With the lighter He–air jet, the jet will retain its integrity and mixing with surrounding air is suppressed. Whereas with the heavier CO_2 jet, the jet will decay fast and mixing is enhanced.

It is well known that conventional linear eddy-viscosity models fail completely to represent the interaction of swirl and density variation, resulting in the solid-body rotation form of the azimuthal velocity profile [6], and always predicting that the central jet mixes rapidly with the surrounding air regardless of its density [7]. In contrast, second moment closures inherently capture the above features acceptably well [3, 8, 9], in which the production rates are represented exactly and the redistribution term (pressure-strain rate correlation tensor) represents mechanisms of the energy redistribution process. However, for the cases studied here, besides the Navier–Stokes and scalar transport equations, second moment closures need to solve a closed system of twelve coupled transport equations governing the distribution of the six independent Reynolds stresses, the three scalar fluxes, the scalar variance, the scalar dissipation rate and the dissipation rate of turbulence energy [9]. Two-equation, cubic eddy-viscosity models offer a better balance between accuracy and cost in many complex flows [10–12]. Some improvements have been achieved with them for constant-density swirling confined flows [13, 14]. With these models, the tangential velocity does not follow the solid-body rotation form any more, but the models still need to develop and calibrate for rotating and swirling flows.

The present study aims at investigating the capability of cubic eddy viscosity turbulence models on strongly swirling flows with variable density. Experiments are conducted by So *et al.* [1], Ahmed and So [4], So and Ahmed [5], in which the central jets of air, He–air, CO_2 is discharged into a coaxial, strongly swirling confined air flow. Two cubic eddy-viscosity turbulence models under low-$Re\,k$–ε framework are Apsley and Leschziner [15] and Merci *et al.* [16]. For comparison, low-$Re\,k$–ε model of Launder and Sharma [17] is chosen as the standard model. All models are compared under the same numerical framework, with the same discretization scheme and iterative solver.

2. GOVERNING EQUATIONS

Variable-density turbulent flows have been studied with various statistical averaging approaches [18], such as Reynolds averaging (or conventional averaging) [19], Favre averaging (or density-weighted averaging, binary regrouping) [20], mixed-weighted decomposition (or transport selected regrouping) [21] and ternary regrouping [22, 23].

Reynolds averaging yields explicit additional contributions arising directly from density fluctuations and possesses clearer physical meaning, however, a very large number of these terms are difficult to model. On the contrary, Favre averaging implicitly consists in density fluctuation correlations into a new macroscopic mean value, and the averaged equations are formally similar to those for constant-density case. This simplification makes Favre averaging be very widely adopted in variable-density flows [3, 7, 9, 24], including turbulent combusting flows [25, 26].

In Favre averaging [20], the mean value of any variable is such that $\tilde{\phi} = \overline{\rho\phi}/\bar{\rho}$ and the fluctuation ϕ'' is such that $\overline{\rho\phi''} = 0$ with $\phi = \tilde{\phi} + \phi''$. Favre averaged fluctuation is not centred, and $\bar{\phi}'' = -\overline{\rho'\phi'}/\bar{\rho} \neq 0$. While in Reynolds averaging $\phi = \bar{\phi} + \phi'$ with $\overline{\phi'} = 0$. The decomposition of density ρ and pressure p are identical in the two methods with $\rho = \bar{\rho} + \rho'$ and $p = \bar{p} + p'$.

For an isothermal, variable density, axisymmetric ($\partial/\partial\theta = 0$) swirling flow in cylindrical co-ordinates, the general form of the governing equations, including the Favre averaged Navier–Stokes equations and the turbulent transport equations, can be expressed as

$$\frac{\partial(\bar{\rho}\phi)}{\partial t} + \frac{\partial}{\partial x}(\bar{\rho}\tilde{U}\phi) + \frac{1}{r}\frac{\partial}{\partial r}(r\bar{\rho}\tilde{V}\phi) - \frac{\partial}{\partial x}\left(\Gamma_\phi \frac{\partial\phi}{\partial x}\right) - \frac{1}{r}\frac{\partial}{\partial r}\left(r\Gamma_\phi \frac{\partial\phi}{\partial r}\right) = S_\phi \tag{1}$$

where t is time. x, r, θ are the axial, radial and tangential co-ordinates, respectively, and $\tilde{U}$, $\tilde{V}$, $\tilde{W}$ are the corresponding mean velocity components. $\bar{\rho}$ is mean fluid density. S_ϕ is the source term and Γ_ϕ is the effective viscosity for the different variables ϕ, as given in Table I.

In Table I, $\Theta = \partial\tilde{U}/\partial x + \partial\tilde{V}/\partial r + \tilde{V}/r$, and $\hat{p} = \bar{p} + (2/3)\bar{\rho}\tilde{k}$. The turbulent eddy-viscosity $\mu_t = \bar{\rho}C_\mu f_\mu \tilde{k}\tau_t$. S_ε is designed to provide the correct near-wall viscous sublayer behaviour.

Table I. The effective viscosity and the source term expressions for the independent variables in Equation (1).

Variable	ϕ	Γ_ϕ	S_ϕ
Mass	1	0	0
Axial momentum (x-direction)	$\tilde{U}$	$\mu + \mu_t$	$-\frac{\partial\hat{p}}{\partial x} + \frac{\partial}{\partial x}\left[\Gamma_\phi\left(\frac{\partial\tilde{U}}{\partial x} - \frac{2}{3}\Theta\right)\right] + \frac{1}{r}\frac{\partial}{\partial r}\left(r\Gamma_\phi\frac{\partial\tilde{V}}{\partial x}\right) + \frac{\partial\tau_{xx}}{\partial x} + \frac{1}{r}\frac{\partial(r\tau_{xr})}{\partial r}$
Radial momentum (r-direction)	$\tilde{V}$	$\mu + \mu_t$	$-\frac{\partial\hat{p}}{\partial r} + \frac{\partial}{\partial x}\left(\Gamma_\phi\frac{\partial\tilde{U}}{\partial r}\right) + \frac{1}{r}\frac{\partial}{\partial r}\left[r\Gamma_\phi\left(\frac{\partial\tilde{V}}{\partial r} - \frac{2}{3}\Theta\right)\right] - \frac{2\Gamma_\phi}{r^2}\left(\tilde{V} - \frac{1}{3}r\Theta\right) + \frac{\bar{\rho}\tilde{W}^2}{r} + \frac{\partial\tau_{rx}}{\partial x} + \frac{1}{r}\frac{\partial(r\tau_{rr})}{\partial r} - \frac{\tau_{\theta\theta}}{r}$
Tangential momentum (θ-direction)	$\tilde{W}$	$\mu + \mu_t$	$-\frac{\bar{\rho}\tilde{V}\tilde{W}}{r} - \frac{\tilde{W}}{r^2}\frac{\partial}{\partial r}(r\Gamma_\phi) + \frac{\partial\tau_{\theta x}}{\partial x} + \frac{1}{r^2}\frac{\partial(r^2\tau_{\theta r})}{\partial r}$
Mixture fraction of jet fluid	$\tilde{F}$	$\rho\kappa + \mu_t/\sigma_F$	0
Turbulent kinetic energy	$\tilde{k}$	$\mu + \mu_t/\sigma_k$	$P_k - \bar{\rho}\tilde{\varepsilon} + G_k$
Dissipation rate	$\tilde{\varepsilon}$	$\mu + \mu_t/\sigma_\varepsilon$	$[C_1 f_1 P_k - C_2 f_2 \bar{\rho}\tilde{\varepsilon} + C_3 G_k]/\tau_t + S_\varepsilon$

The production rate of the turbulent kinetic energy

$$P_k = -\overline{\rho u_i'' u_j''} \frac{\partial \tilde{U}_i}{\partial x_j} = -\bar{\rho}\tilde{\varepsilon} a_{ij} s_{ij} \tag{2}$$

G_k denotes additional production resulting from the coupling of the turbulent mass flux with the mean pressure field. It is briefly called the mean pressure work, and is specific to variable density flows and Favre formulation [27],

$$G_k = -\overline{u_i''} \frac{\partial \bar{p}}{\partial x_i} \tag{3}$$

For the case of binary inert mixing at the same pressure and temperature, according to the equation of state, the specific volume is a linear function of a conserved scalar [28], which is chosen as the mixture fraction of jet fluid, denoted by F

$$\frac{1}{\rho} = aF + b \tag{4}$$

where a, b are constants, and $a = (\rho_a - \rho_j)/\rho_a\rho_j$, $b = 1/\rho_a$.

Favre averaging yields

$$\frac{1}{\bar{\rho}} = a\tilde{F} + b \tag{5}$$

If this equation is subtracted from Equation (4), there follows

$$\rho' = -a\rho\bar{\rho} f'' \tag{6}$$

This relation allows an exact expression for $\bar{\phi}''$ to be obtained [9],

$$\bar{\phi}'' = -\frac{\overline{\rho'\phi'}}{\bar{\rho}} = -\frac{\overline{\rho'\phi''}}{\bar{\rho}} = \frac{a\bar{\rho}\overline{\rho\phi'' f''}}{\bar{\rho}} = a\overline{\rho\phi'' f''} \tag{7}$$

The turbulent mass flux is expressed as

$$\overline{u_i''} = a\overline{\rho u_i'' f''} \tag{8}$$

With the assumption of turbulent scalar flux

$$\overline{\rho u_i'' f''} = -\frac{\mu_t}{\sigma_F} \frac{\partial \tilde{F}}{\partial x_i} \tag{9}$$

then the mean pressure work

$$G_k = -\overline{u_i''} \frac{\partial \bar{p}}{\partial x_i} = -a\overline{\rho u_i'' f''} \frac{\partial \bar{p}}{\partial x_i} = a \frac{\mu_t}{\sigma_F} \frac{\partial \tilde{F}}{\partial x_i} \frac{\partial \bar{p}}{\partial x_i} \tag{10}$$

From Equation (5), there follows

$$\frac{\partial \tilde{F}}{\partial x_i} = -\frac{1}{a} \frac{1}{\bar{\rho}^2} \frac{\partial \bar{\rho}}{\partial x_i} \tag{11}$$

The mean pressure work

$$G_k = a\,\frac{\mu_t}{\sigma_F}\,\frac{\partial \tilde{F}}{\partial x_i}\,\frac{\partial \bar{p}}{\partial x_i} = -\frac{\mu_t}{\sigma_F}\,\frac{1}{\bar{\rho}^2}\,\frac{\partial \bar{\rho}}{\partial x_i}\,\frac{\partial \bar{p}}{\partial x_i} \tag{12}$$

which is adopted in the model of Merci *et al.* [16].

Rotating motion inhibits the transfer of energy from the large to the small scales. The dissipation rate equation should contain some explicit dependence on swirl level in a manner so as to reduce the dissipation rate as swirl is increased [29]. The modification of the dissipation rate equation was originally developed for the rotating homogeneous flows without mean rate of strain by Bardina *et al.* [30].

$$C_2 = 1.83 + 0.15\Omega^* \tag{13}$$

where $\Omega^* = (k/\varepsilon)\sqrt{\Omega_k \Omega_k}$, and Ω_k is the system angular velocity.

For more general wall-bounded rotating and swirling flows, Bardina *et al.* [30] proposed to replace Ω^* by $\sqrt{w_{kl}w_{kl}/2}$, that is

$$C_2 = 1.83 + 0.075\bar{w} \tag{14}$$

However, such a term remain active also in flows without rotation, and it would deteriorate the predictions of flows [31]. Considering the effect of high strain rates, Merci *et al.* [16] proposed

$$C_2 = 1.83 + \frac{0.075\bar{w}}{1 + \bar{s}^2} \tag{15}$$

which is used in the present study.

3. CUBIC EDDY-VISCOSITY MODELS

The dimensionless Reynolds-stress anisotropy tensor is defined by

$$a_{ij} = \frac{\overline{\rho u_i'' u_j''}/\bar{\rho}}{\tilde{k}} - \frac{2}{3}\,\delta_{ij} \tag{16}$$

Although the foundation and derivation of different models can differ greatly, for non-linear eddy-viscosity models up to cubic order, the stress–strain relationship may be written in the following canonical form:

$$a_{ij} = -2C_\mu f_\mu s_{ij} + A_{ij} \tag{17}$$

$$\begin{aligned} A_{ij} = {} & \beta_1(s_{ik}s_{kj} - \tfrac{1}{3}\,s_{kl}s_{kl}\delta_{ij}) + \beta_2(w_{ik}s_{kj} - s_{ik}w_{kj}) + \beta_3(w_{ik}w_{kj} + \tfrac{1}{3}\,w_{kl}w_{kl}\delta_{ij}) \\ & -\gamma_1 s_{kl}s_{kl}s_{ij} + \gamma_2 w_{kl}w_{kl}s_{ij} - \gamma_3(w_{ik}w_{kl}s_{lj} + s_{ik}w_{kl}w_{lj} + w_{kl}w_{kl}s_{ij} - \tfrac{2}{3}\,w_{kj}s_{lm}w_{mk}\delta_{ij}) \\ & -\gamma_4(w_{ik}s_{kl}s_{lj} - s_{ik}s_{kl}w_{lj}) \end{aligned} \tag{18}$$

Table II. Abbreviations for different turbulence models.

Model	Abbreviation
Launder and Sharma [17]	SKE
Apsley and Leschziner [15]	AL
AL with Equation (15)	AL-M
AL-M with G_k (Density effects term)	AL-M-D
Merci *et al.* [16]	MDVD-D
Merci *et al.* without G_k	MDVD

Table III. Model coefficients in the turbulent transport equations.

Model	C_μ	C_1	C_2	C_3	σ_F	σ_k	σ_ε
SKE	0.09	1.44	1.92	1.0	0.9	1.0	1.3
AL	Equation (22)	1.44	1.83	1.0	0.9	Equation (29)	Equation (29)
MDVD-D	Equation (32)	1.44	Equation (15)	1.0	0.9	1.0	1.3

The quadratic terms and the strain/vorticity-dependent coefficients are responsible for the ability of non-linear models to capture anisotropy, and the cubic terms can reflect the effect of curvature [10]. The cubic term can also capture the swirling effect [32].

The non-linear part of the Reynolds stresses:

$$\tau_{ij} = -\bar{\rho}\tilde{k}A_{ij} \tag{19}$$

The components of dimensionless mean strain and mean vorticity tensors are denoted by

$$\begin{aligned}
&s_{11} = \tau_t\left(\frac{\partial\tilde{U}}{\partial x} - \frac{1}{3}\Theta\right), \quad s_{12} = \frac{\tau_t}{2}\left(\frac{\partial\tilde{U}}{\partial r} + \frac{\partial\tilde{V}}{\partial x}\right), \quad s_{13} = \frac{\tau_t}{2}\frac{\partial\tilde{W}}{\partial x}\\
&s_{22} = \tau_t\left(\frac{\partial\tilde{V}}{\partial r} - \frac{1}{3}\Theta\right), \quad s_{23} = \frac{\tau_t}{2}\left(\frac{\partial\tilde{W}}{\partial r} - \frac{\tilde{W}}{r}\right), \quad s_{33} = \tau_t\left(\frac{\tilde{V}}{r} - \frac{1}{3}\Theta\right)\\
&w_{12} = \frac{\tau_t}{2}\left(\frac{\partial\tilde{U}}{\partial r} - \frac{\partial\tilde{V}}{\partial x}\right), \quad w_{13} = -\frac{\tau_t}{2}\frac{\partial\tilde{W}}{\partial x}, \quad w_{23} = -\frac{\tau_t}{2}\left(\frac{\partial\tilde{W}}{\partial r} + \frac{\tilde{W}}{r}\right)
\end{aligned} \tag{20}$$

Note that $s_{ij} = s_{ji}$ and $w_{ij} = -w_{ji}$.

Abbreviations for different turbulence models are listed in Table II. Model coefficients in $\tilde{k}$ and $\tilde{\varepsilon}$ turbulent transport equations of different models are given in Table III.

3.1. *Apsley and Leschziner (1998)* [15]

The stress–strain relationship is formed by successive iterative approximations to an algebraic Reynolds-stress model. Free coefficients are calibrated by reference to DNS data for a channel flow.

The turbulence time scale is

$$\tau_t = \frac{\tilde{k}}{\tilde{\varepsilon}} \tag{21}$$

$$C_\mu = \frac{-a_{12}^* f_P}{(1 + \bar{\beta}^2/3 - \bar{\gamma}^2)\sigma^*} \tag{22}$$

$$\beta_1 = 6(a_{11}^* + a_{22}^*)(f_P/\sigma^*)^2, \quad \beta_2 = (a_{11}^* - a_{22}^*)(f_P/\sigma^*)^2, \quad \beta_3 = 0;$$

$$\gamma_1 = \tfrac{4}{3} C_\mu \bar{\beta}^2 (f_P/\sigma^*)^2, \quad \gamma_2 = 4C_\mu \bar{\gamma}^2 (f_P/\sigma^*)^2$$

$$\gamma_3 = 6C_\mu \bar{\gamma}^2 (f_P/\sigma^*)^2, \quad \gamma_4 = 6C_\mu \bar{\beta}\bar{\gamma} (f_P/\sigma^*)^2 \tag{23}$$

$$f_\mu = f_1 = f_2 = 1 \tag{24}$$

$$S_\varepsilon = C_2 f_2 \frac{\varepsilon^{(1)}\tilde{\varepsilon}}{\tilde{k}} \exp(-0.0038 y^{*2}), \quad \varepsilon^{(1)} = \frac{C_\mu^{*3/4}\tilde{k}^{3/2}}{l_\varepsilon^{(1)}}, \quad C_\mu^* = 0.09 \tag{25}$$

$$\bar{\beta} = 0.222, \quad \bar{\gamma} = 0.623 \tag{26}$$

The dissipation length is based on the results of DNS data:

$$l_\varepsilon^{(1)} = 0.179 y_n (1 + 128/y^*)[1 - \exp(-y^{*2}/279)] \tag{27}$$

where y_n is the distance from the nearest wall and $y^* \equiv y_n \sqrt{\tilde{k}}/\nu$ is a dimensionless distance.

The anisotropy-tensor components a_{ij}^* and the shear parameter σ^* in equilibrium condition are calibrated from DNS data for plane channel flow:

$$\begin{aligned} a_{11}^* &= 1 + 0.42 \exp\left(0.296\sqrt{y^*} - 0.040 y^*\right) - 2/3 \\ a_{22}^* &= 0.404[1 - \exp(-0.001 y^* - 0.000147 y^{*2})] - 2/3 \\ a_{12}^* &= -0.3\left[1 - \exp\left(-0.00443\sqrt{y^*} - 0.0189 y^*\right)\right] \\ \sigma^* &= 3.33[1 - \exp(-0.45 y^*)][1 + 0.277 y^{*3/2} \exp(-0.088 y^*)] \end{aligned} \tag{28}$$

The constants in turbulent transport equations are:

$$C_1 = 1.44, \quad C_2 = 1.83, \quad \sigma_k = \frac{1.0}{1 + \bar{\beta}^2/3 - \gamma^2}, \quad \sigma_\varepsilon = \frac{1.37}{1 + \bar{\beta}^2/3 - \bar{\gamma}^2} \tag{29}$$

The non-equilibrium parameter, which accounts for departures of the local shear parameter $\sigma = \sqrt{s_{kl}s_{kl} + w_{kl}w_{kl}}$, is

$$\begin{aligned} f_P &= \frac{2 f_0}{1 + \sqrt{1 + 4 f_0 (f_0 - 1)(\sigma/\sigma^*)^2}} \\ f_0 &= 1 + 1.25 \max(0.09\sigma^{*2}, 1.0) \end{aligned} \tag{30}$$

3.2. *Merci et al.* (*2001*) [16]

This cubic model combined with a new transport equation for the dissipation rate, in which a low-Reynolds source term is introduced. The model has been checked on different realizability constraints.

The turbulence time scale in this low-Reynolds model is defined as

$$\tau_t = \frac{\tilde{k}}{\tilde{\varepsilon}} + \sqrt{\frac{\mu}{\bar{\rho}\tilde{\varepsilon}}} \tag{31}$$

$$C_\mu = (A_1 + A_s \max(\bar{s}, \bar{w}))^{-1} \tag{32}$$

where the dimensionless strain invariant and vorticity invariant can be written as

$$\bar{s} \equiv \sqrt{2s_{kl}s_{kl}}, \quad \bar{w} \equiv \sqrt{2w_{kl}w_{kl}} \tag{33}$$

$$A_1 = 8, \quad A_s = \sqrt{3}\cos\phi, \quad \phi = \tfrac{1}{3}\arccos(\sqrt{6}W), \quad W = 2^{1.5}\frac{s_{ij}s_{jk}s_{ki}}{\bar{s}^3} \tag{34}$$

$$\beta_1 = q_1, \quad \beta_2 = q_2 + q_1/6, \quad \beta_3 = 0, \quad \gamma_1 = \gamma_2 = -c, \quad \gamma_3 = 0, \quad \gamma_4 = 2c \tag{35}$$

$$q_1 = (7 + 3\max(\bar{s}, \bar{w}) + 1.2 \times 10^{-2}\max(\bar{s}^3, \bar{w}^3))^{-1}$$

$$q_2 = (1.7 + 5.4\max(\bar{s}, \bar{w}) + 3 \times 10^{-2}\max(\bar{s}^3, \bar{w}^3))^{-1}$$

$$\bar{s} \geqslant \bar{w}, \quad c = -600C_\mu^4; \quad \bar{s} < \bar{w}, \quad c = -\min(600C_\mu^4; 4f_\mu C_\mu/(\bar{w}^2 - \bar{s}^2)) \tag{36}$$

$$f_\mu = 1 - \exp\left(-4.2 \times 10^{-2}\sqrt{y^*} - 5.1 \times 10^{-4}y^{*1.5} - 3.65 \times 10^{-10}y^{*5}\right)$$

$$f_1 = 1, \quad f_2 = 1 - 0.22\exp\left(-\frac{Re_t^2}{36}\right) \tag{37}$$

where $Re_t = \bar{\rho}\tilde{k}\tau_t/\mu$ is the turbulence Reynolds number.

The cross diffusion term, which only has an influence near the wall, is added in the low-Reynolds formulation

$$S_\varepsilon = -1.8(1 - f_\mu)(\mu + \mu_t/\sigma_\varepsilon)\frac{\partial\tilde{k}}{\partial x_i}\frac{\partial\tau_t^{-1}}{\partial x_i} \tag{38}$$

4. NUMERICAL METHOD

All computations are performed by the same code based on the finite volume method with non-orthogonal grids [33]. Variable storage is co-located and cell-centred, with Rhie–Chow

interpolation for cell-face mass fluxes. The SIMPLE pressure-correction algorithm is used to obtain the pressure field. For the discretization of the convective fluxes, the deferred correction technique with a blended upwind-central differencing scheme is used. The diffusion terms are approximated by the second-order central differencing scheme. For all variables, the blending factor of central differencing is 0.0 (pure upwind scheme) in the beginning, and then 0.5 to the end. The Stone's SIP (strongly implicit procedure) method is employed with under-relaxation factors.

Convergence is judged by monitoring the magnitude of the absolute residual sources of mass and momentum, normalized by the respective inlet fluxes. The iteration is continued until all above residuals fell below 0.05%.

5. RESULTS AND DISCUSSIONS

5.1. Geometry and boundary conditions

The flow geometry is shown in Figure 1. A strongly swirling outer air flow, characterized by the swirl number

$$S = \int_0^R UWr^2 \,\mathrm{d}r \Big/ R \int_0^R U^2 r \,\mathrm{d}r = 2.25 \tag{39}$$

is introduced into a chamber of radius $R = 62.5$ mm together with a central nonswirling jet of diameter $d = 8.73$ mm. The central jet fluid is air, He–air, and CO_2, respectively. The overall average velocity upstream of swirler U_{av} is about 6.8 m/s. Based on U_{av} and the diameter of the test section, the characteristic Reynolds number, was $Re = 5.49 \times 10^4$. All experiments are carried out at this one Reynolds number. Test conditions for different jet fluids are summarized in Table IV. The parameters ρ_j/ρ_a, U_j, Re_j and $\dot{M}_j/\dot{M}$ denote jet fluid to swirling air density ratio, jet velocity, jet Reynolds number based on U_j and jet nozzle diameter d, and jet to swirling flow axial momentum ratio, respectively.

The scalar measured in experiments is volume concentration C of He [4]. However, the scalar calculated is the mixture fraction of jet fluid, $\tilde{F}$. Therefore, C are transformed into $\tilde{F}$

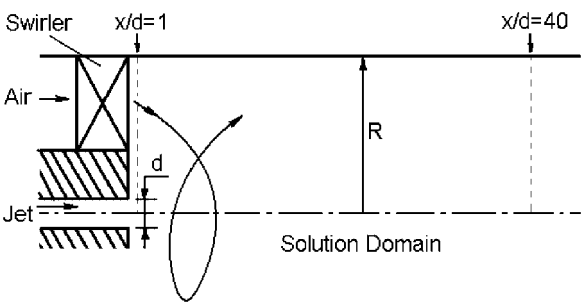

Figure 1. Geometry of strongly swirling confined flow.

Table IV. Test conditions of gas jet experiments.

Parameters	Air jet	He–air jet	CO_2 jet
ρ_j/ρ_a	1	0.31	1.52
U_j (m/s)	25.4	16.8	25.4
$Re_j \times 10^{-3}$	14.38	1.50	28.43
$\dot{M}_j/\dot{M}$	0.068	0.009	0.104

with the aid of a β probability density function (PDF) $P(C)$ for C [9],

$$\tilde{F} = \int F(C)P(C)\,\mathrm{d}C \tag{40}$$

where $F = F(C)$ is the instantaneous relationship between F and C.

As shown in Figure 1, the solution domain is bounded by inlet plane, confining wall, axis of symmetry and exit plane. The inlet plane is located at $x/d = 1$, where the measured data for $\tilde{U}$, $\tilde{W}$, $\tilde{F}$ are specified, and $\tilde{V} = 0$. For CO_2 jet case, in the absence of information for the scalar field, the measured $\tilde{F}$ profile of He–air jet is used. The turbulent kinetic energy $\tilde{k}$ is calculated from the measured and assumed normal stresses. The dissipation rate is estimated from

$$\tilde{\varepsilon} = C_\mu^{3/4}\tilde{k}^{3/2}/L \tag{41}$$

where the length scale $L = 0.06R$ [3]. At the wall, $\tilde{U}$, $\tilde{V}$, and $\tilde{W}$ are set to zero according to the wall no-slip conditions. Zero-gradient condition is adopted for $\tilde{F}$. $\tilde{k}_w = 0$, $\tilde{\varepsilon}_w = 2\nu\tilde{k}_p/y_p^2$, where subscript w denotes the value at the wall and subscript p the value at the near-wall node. At the axis of symmetry, zero-gradient conditions are adopted for all variables except $\tilde{V}$ and $\tilde{W}$, which are set to zero. Because of the subcritical nature of the flow, at the exit plane $x/d = 40$, the measured axial velocity $\tilde{U}$ is prescribed to avoid the predictive uncertainties [8]. Zero-gradient conditions are adopted for other variables. For CO_2 jet case, $\tilde{U}$ is set to zero in the backward velocity region near the axis of symmetry to use zero-gradient conditions for other variables [9].

5.2. Grid independency

The grid with 150×170 cells is employed, which is fine enough to minimize the effects of numerical diffusion [34] and the solutions are virtually indistinguishable from those obtained by pure upwind differencing. This non-uniform grid ensures $y^+ < 0.1$ along the first grid-line from the wall for the use of low-Reynolds-number turbulence models. The grid is also refined near the symmetry plane where large density gradient is encountered.

To prove grid-independency, grids with 75×85 and 300×340 cells are also adopted. Figure 2 shows the profiles of axial and azimuthal velocities for air jet calculated by SKE model with these three grids. The results show that the grid with 150×170 cells is sufficient to ensure grid-independence.

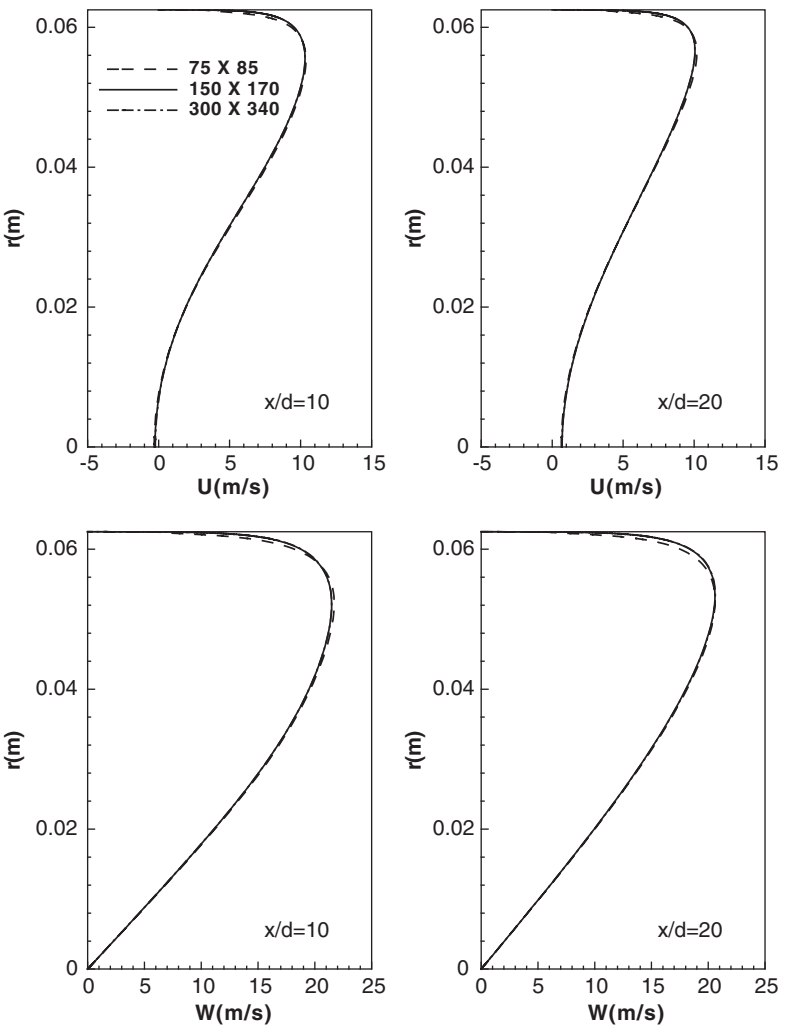

Figure 2. Axial and azimuthal velocity profiles with grid refinement.

5.3. *Air jet*

Figure 3 shows the decay of centerline axial velocity with different models. SKE predicts a reserve flow region. AL and AL-M perform like SKE although there are no recirculation regions. They seriously overestimate the levels of shear stress throughout the domain, resulting in the rapid disappearance of central jet. MDVD is in closest agreement with the measurements, and captures the subcritical nature of the flow very well. The oscillation of the profile around $x/d = 4$ for MDVD is due to the sensitivity to inlet condition $\tilde{V} = 0$.

Figure 4 represents the axial velocity profiles at different locations. The results of AL and AL-M are almost identical except near the centreline, so that the rotation modification to the ε equation is negligible. SKE, AL and AL-M are in reasonable agreement with experimental

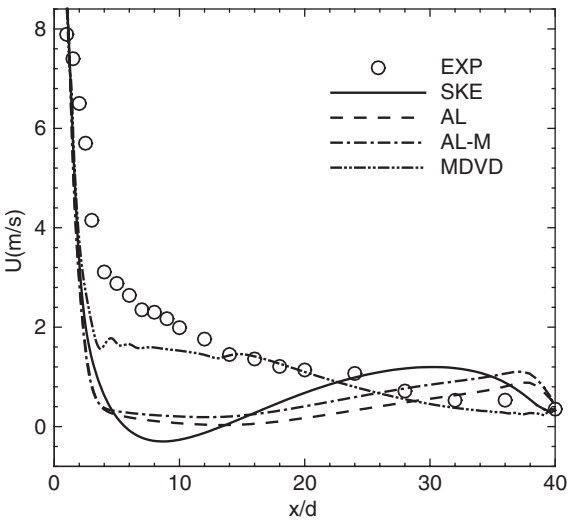

Figure 3. Centreline axial velocity for air jet.

data in the outer region, however, they predict a rapid decay of jet near the centreline. It is clear that MDVD predicts the decay of central jet correctly, but the profiles have a radial displacement and the overall agreement is not satisfied.

The radial profiles of the azimuthal velocity are shown in Figure 5. SKE predicts a solid body profile of the azimuthal velocity. Whereas AL and AL-M mimic the observed combined forced-free vortex motion, and agree with measurements fairly well. However, MDVD fails to predict the azimuthal velocity. It is indicated that the fully developed rotating pipe flow does not contain enough flow physics to calibrate the cubic turbulence model, hence the calibration of cubic terms is still a topic of investigation [14].

5.4. He–air jet

The decay of centreline axial velocity for He–air jet is given in Figure 6. The results are similar to those of air jet. SKE, AL-M and AL-M-D predict recirculation bubbles near the jet nozzle. MDVD-D agrees with experimental data fairly well, predicting the combined stabilizing effect of swirl and density difference, whereas MDVD overestimates the decay to some extent. The mean pressure work term G_k, representing the coupling of the turbulent mass flux with the mean pressure field, exerts a significant influence on the computed results, and cannot be neglected.

The decay of mixture fraction at centreline is shown in Figure 7. SKE, AL-M and AL-M-D predict a rapid decay of mixture fraction due to the reserve flow region at the axis of symmetry, resulting in a rapid mixing between jet fluid and surrounding air. MDVD-D is close to the measurements to some extent, similar to the results of second moment closures [9]. MDVD predicts a much more rapid decay. The interaction between density gradients and swirl induced pressure gradients is importance here, and should be modeled.

Figure 8 represents the radial profiles of the axial velocity at different locations. SKE and AL-M-D predict recirculation regions at the axis of symmetry and enhance the mixing of jet

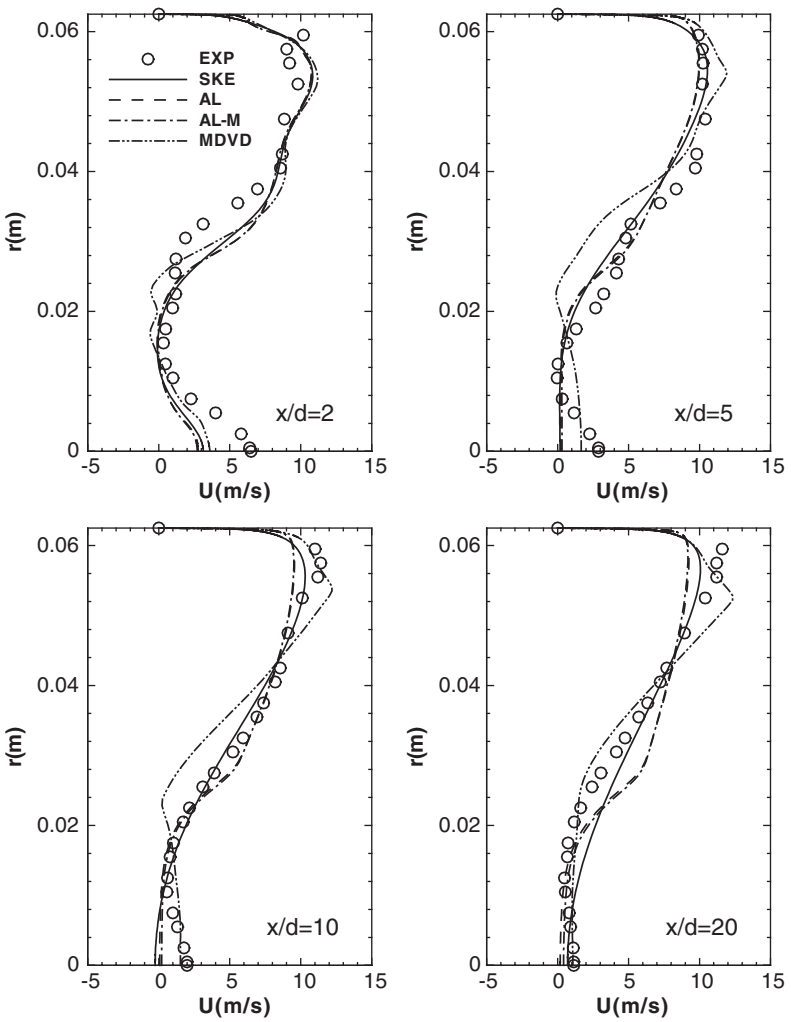

Figure 4. Axial velocity profiles for air jet.

fluid. MDVD-D successfully represents the central jet decay and agrees with experimental data very well near the axis of symmetry. Without the term of mean pressure work, MDVD fails to capture the behavior of central jet decay. MDVD-D also predicts a recirculation bubble between the jet fluid and the outer swirling air flow, which serves as a buffer to suppress the mixing and is correspond to the experiments, although the predicted profiles have a radial outside displacement. MDVD-D improves the results of MDVD also in this region.

Figure 9 shows the azimuthal velocity profiles. The results are similar to those of air jet. SKE predicts a solid body rotation. AL-M-D agrees with experimental data well at $x/d = 5$, 10 and 20, where MDVD and MDVD-D fail to predict correctly. At $x/d = 40$, MDVD and MDVD-D show better results because the flow is nearly fully developed. The results of MDVD

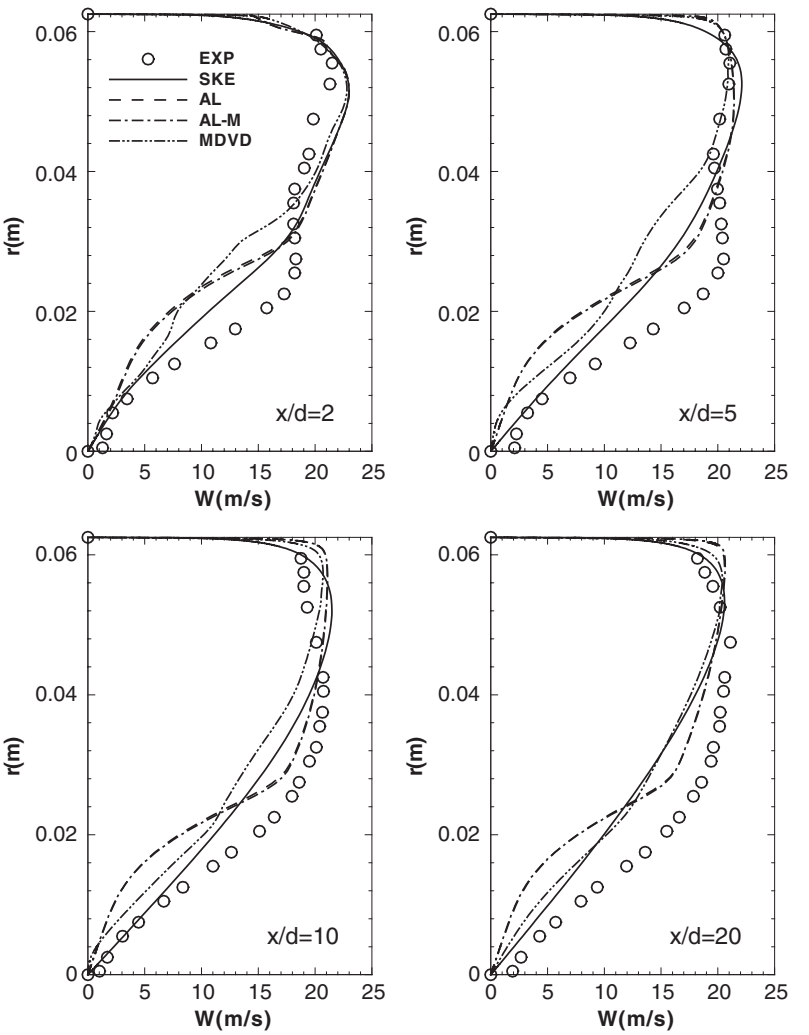

Figure 5. Azimuthal velocity profiles for air jet.

and MDVD-D show that the mean pressure work term has little influence on the azimuthal velocity.

Figure 10 gives the mixture fraction profiles for He–air jet at different locations. SKE, AL-M-D completely fail to predict the mixing of central jet, representing a uniform profile of sufficient mixing, which is due to the central recirculation bubbles predicted. MDVD gives a rapid decay of central jet. MDVD-D gives results similar to second moment closures [9]. Although the peak values at the axis of symmetry are not correspond to the measurements, the boundary of He–air jet region is predicted very well, since MDVD-D represents the recirculation region between the jet fluid and the outer swirling air flow correctly.

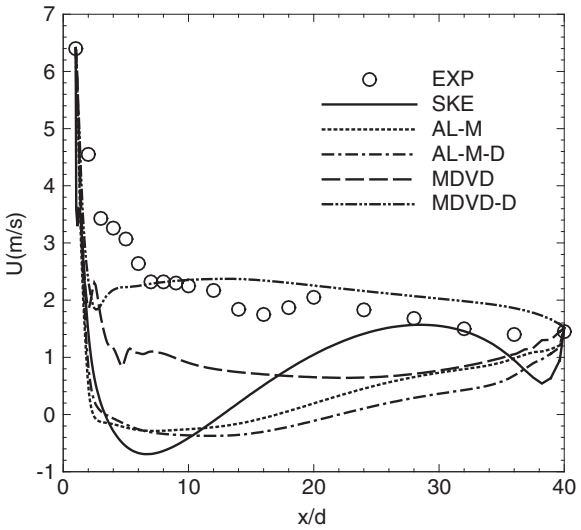

Figure 6. Centreline axial velocity for He–air jet.

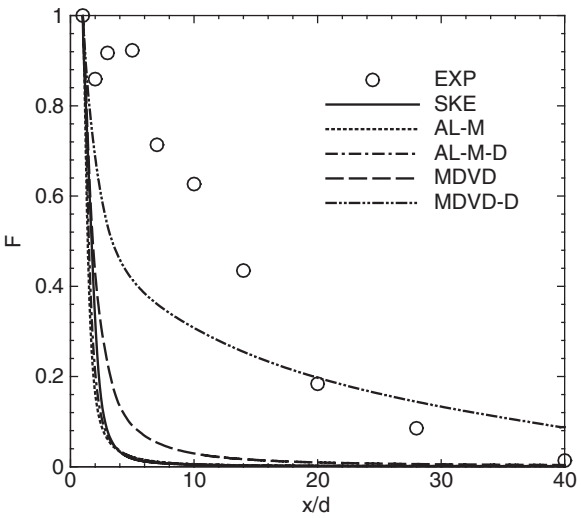

Figure 7. Centreline mixture fraction for He–air jet.

5.5. CO_2 *jet*

Figure 11 represents the decay of centreline axial velocity for CO_2 jet. SKE, AL-M, and AL-M-D predict central recirculation bubbles near the jet nozzle. However, experiments show that the central recirculation bubble appears downstream. MDVD and MDVD-D predict correct decay of central jet. The mean pressure work term is found to be small in the present case and exert a negligible influence on the computed results.

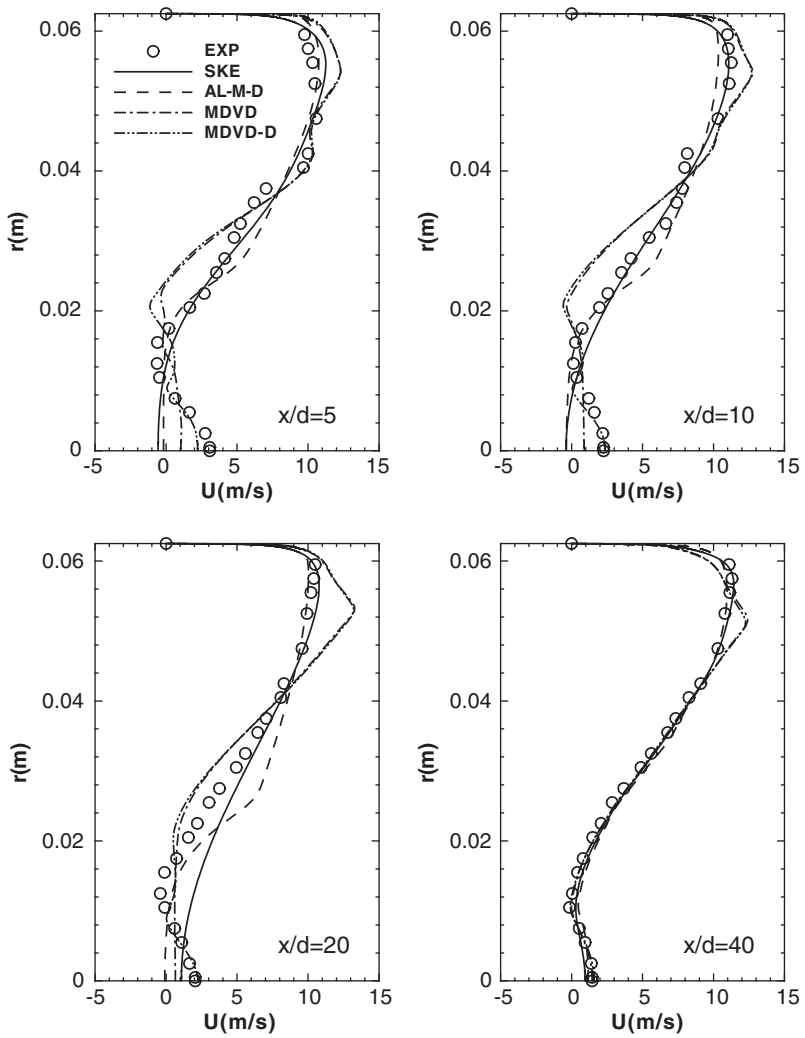

Figure 8. Axial velocity profiles for He–air jet.

The decay of mixture fraction at centreline is shown in Figure 12. Contrary to the results in He–air jet, density difference and swirl combined give rise to an accelerated decay of the jet and increased mixing between jet fluid and the outer swirling air flow. Without the central recirculation, MDVD and MDVD-D predict a slower decay of central jet than other models.

Figure 13 shows the axial velocity profiles. There are almost no difference between MDVD and MDVD-D, which predict the central decay better than other models. SKE and AL-M-D predict reserve regions near the axis of symmetry, while MDVD and MDVD-D predict recirculation bubbles between the jet fluid and the outer swirling air flow, which are incorrect compared with the measurements. Figure 14 represents the azimuthal velocity profiles. The results are similar to those of He–air jet.

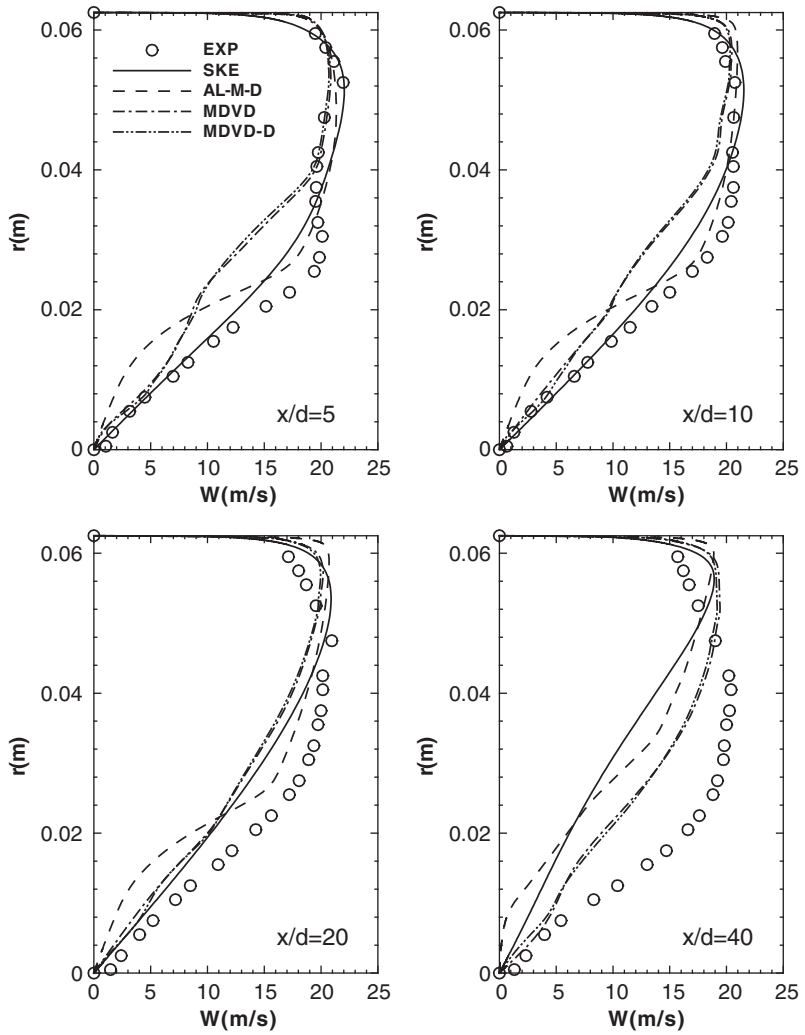

Figure 9. Azimuthal velocity profiles for He–air jet.

6. CONCLUSIONS

The present studies show that the cubic models give some improvements compared to SKE in the prediction of strongly swirling flows with variable density. SKE does not contain any mechanism to represent the interaction of swirl and density variation and as a consequence it performs poorly, predicting the solid-body rotation and rapid decay of central jet regardless of its density. Cubic model of Merci *et al.* [16] captures the subcritical nature of the flow and predicts the combined effects of swirl and density variation successfully. It predicts the rapid decay of the CO_2 jet and the much slower decay of the He–air jet correctly, although it cannot exactly represent the azimuthal velocity. Cubic model of Apsley and Leschziner [15]

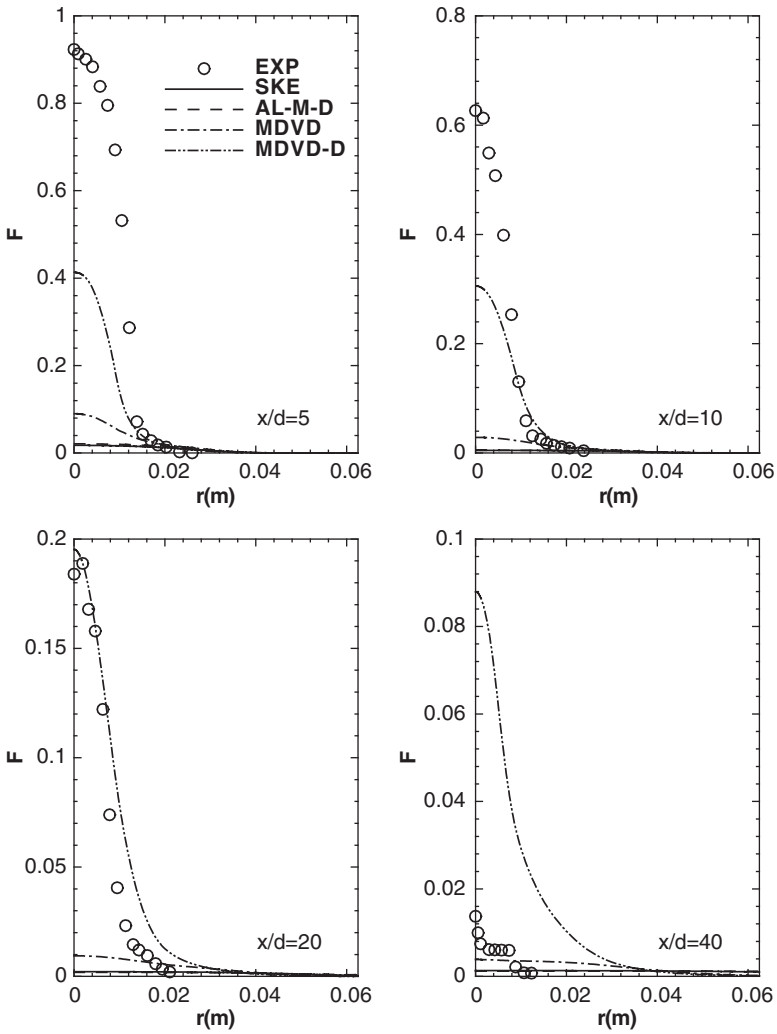

Figure 10. Mixture fraction profiles for He–air jet.

represents the azimuthal velocity profiles of combined forced-free vortex motion fairly well, however, it overestimates the decay of central jet to some extent. These results show that cubic models can represent the flow physics well with appropriate modelling, and the calibration of model coefficients is still a topic of investigation. The linear assumption Equation (9) cannot represent the anisotropy of turbulent scalar flux, and non-linear models for the turbulent scalar flux are necessary [35].

The redistribution term in second moment closures represents mechanisms of the energy redistribution process, which associates with non-local interactions due to the pressure fluctuations, and is a key element in capturing complex flow phenomena, such as the effects of swirling and rotation. Unfortunately, the redistribution term has no counterpart in the kinetic

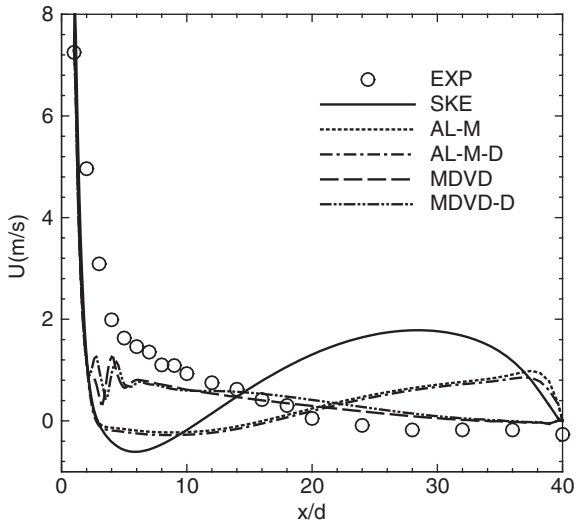

Figure 11. Centreline axial velocity for CO_2 jet.

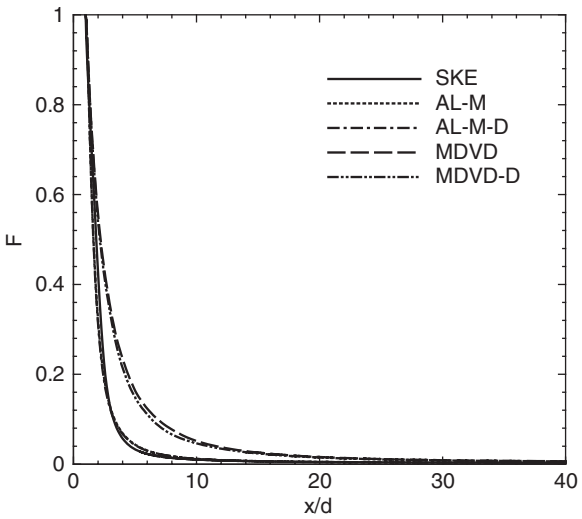

Figure 12. Centreline mixture fraction for CO_2 jet.

energy equation, since it has zero trace. It is also known that the proposed ε-equation used so far suffer from the lack of detailed justification [36]. For k–ε two-equation cubic turbulence models, further amendments are needed for the equations of k and ε to take into account the effects of swirl and density gradients.

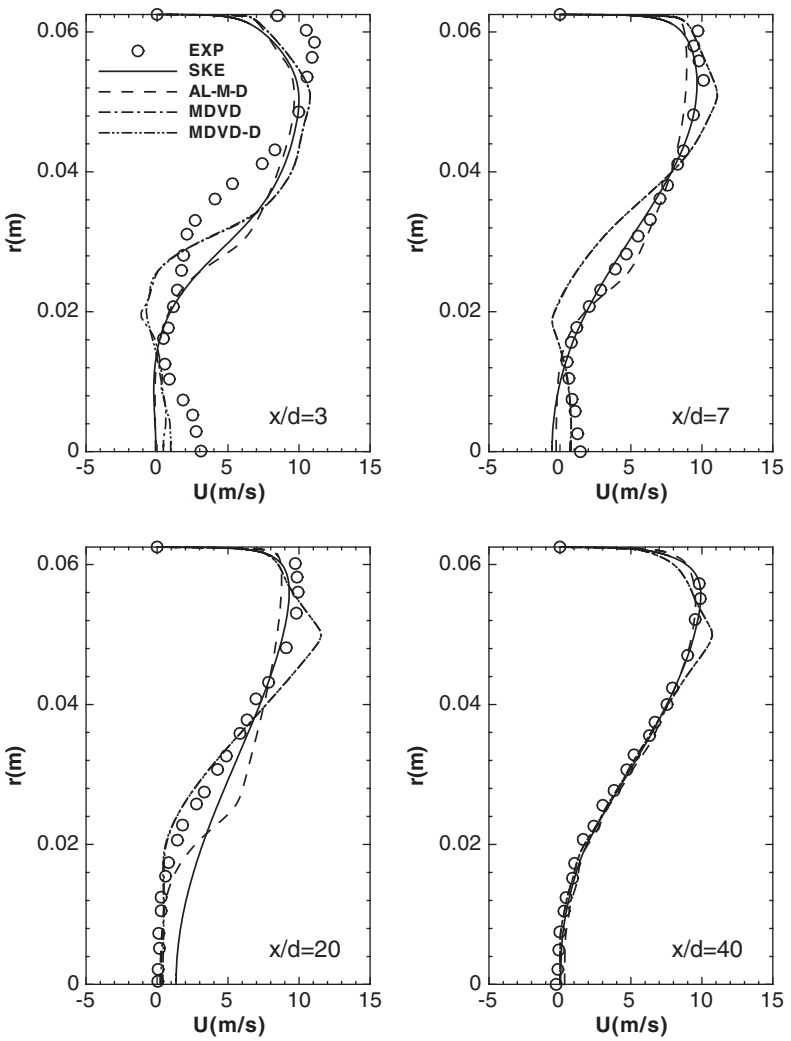

Figure 13. Axial velocity profiles for CO_2 jet.

NOMENCLATURE

a, b	constants in scalar density relation
a_{ij}	dimensionless Reynolds-stress anisotropy tensor
A_{ij}	non-linear part of a_{ij}
C	volume concentration
C_1, C_2, C_3	model coefficients
C_μ	eddy viscosity coefficient
d	jet nozzle diameter
F	mixture fraction of jet fluid

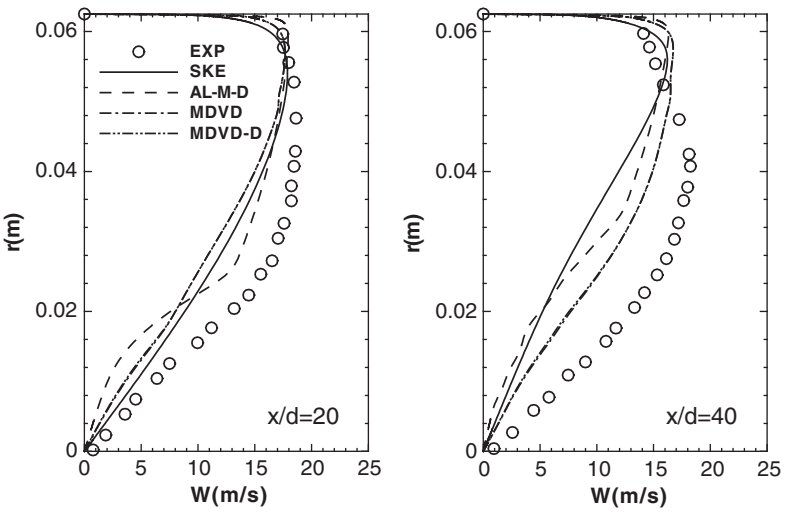

Figure 14. Azimuthal velocity profiles for CO_2 jet.

$\tilde{F}$	Favre averaged mixture fraction
f''	Favre averaged fluctuating mixture fraction
f_1, f_2, f_μ	wall damping functions
G_k	mean pressure work
k	turbulent kinetic energy
$\tilde{k}$	Favre averaged turbulent kinetic energy ($\equiv (1/2)\overline{\rho u_i'' u_i''}/\bar{\rho}$)
$\dot{M}$	axial momentum flux of swirling flow ($\equiv \int_0^R 2\pi U^2 r \, dr$)
$\dot{M}_j$	jet momentum flux ($\equiv \frac{1}{4}\pi d^2 U_j^2$)
p	static pressure
P_k	production rate of the turbulent kinetic energy
r	radial distance
R	radius of combustor
Re	Reynolds number
Re_j	jet Reynolds number
Re_t	turbulence Reynolds number
S	swirl number
s_{ij}	dimensionless mean strain tensor
S_ε	near-wall viscous term
S_ϕ	source term for ϕ
$\bar{s}$	dimensionless strain invariant ($\equiv \sqrt{2 s_{kl} s_{kl}}$)
t	time
$\tilde{U}, \tilde{V}, \tilde{W}$	Favre averaged axial, radial, and azimuthal velocities
u_i''	Favre averaged fluctuating velocity
U_av	overall average velocity upstream of swirler
w_{ij}	dimensionless mean vorticity tensor
$\bar{w}$	dimensionless vorticity invariant ($\equiv \sqrt{2 w_{kl} w_{kl}}$)

x	axial distance
x_i	co-ordinate vector ($x_1 = x,\ x_2 = r$)
y^*	dimensionless wall distance

Greek symbols

$\beta_1, \beta_2, \beta_3$	coefficients for quadratic terms of Reynolds stresses
ε	dissipation rate of turbulent kinetic energy
$\tilde{\varepsilon}$	favre averaged dissipation rate of turbulent kinetic energy ($\equiv \overline{T_{ij}\partial u_i''/\partial x_j}/\bar{\rho}$, T_{ij} is molecular viscous stress tensor)
ϕ	independent variable
Γ_ϕ	effective viscosity for ϕ
$\gamma_1, \gamma_2, \gamma_3, \gamma_4$	coefficients for cubic terms of Reynolds stresses
κ	diffusion coefficient
μ	molecular kinetic viscosity
μ_t	turbulent eddy viscosity
ν	molecular kinematic viscosity
θ	azimuthal angle
Θ	divergence of velocity
ρ	fluid density
$\sigma_F,\ \sigma_k,\ \sigma_\varepsilon$	turbulent Schmidt number
τ_{ij}	non-linear part of Reynolds stresses
τ_t	turbulence time scale
Ω_k	system angular velocity

Subscripts

a	air
j	jet
p	near-wall node
t	turbulent
w	wall
x, r, θ	axial, radial, and azimuthal co-ordinates
ϕ	independent variable

Superscripts

-	Reynolds averaged quantity
~	Favre averaged quantity
$'$	Reynolds averaged fluctuation
$''$	favre averaged fluctuation

ACKNOWLEDGEMENTS

The financial support provided by the National Natural Science Foundation of China (50076043) is gratefully acknowledged. Particular thanks are due to Professors R. M. C. So, A. Pascau, M. A. Leschziner, T.-H. Shih, D. Wennerberg, and Doctor B. Merci for valuable discussions.

REFERENCES

1. So RMC, Ahmed SA, Mongia HC. An experimental investigation of gas jets in confined swirling air flow. *NASA CR* 3832, 1984.
2. Escudier MP, Keller JJ. Recirculation in swirling flow: a manifestation of vortex breakdown. *AIAA Journal* 1985; **23**:111–116.
3. Hogg S, Leschziner MA. Second-moment-closure calculation of strongly swirling confined flow with large density gradients. *International Journal of Heat and Fluid Flow* 1989; **10**(1):16–27.
4. Ahmed SA, So RMC. Concentration distributions in a model combustor. *Experiments in Fluids* 1986; **4**:107–113.
5. So RMC, Ahmed SA. Behaviour of carbon dioxide jets in a confined swirling flow. *International Journal of Heat and Fluid Flow* 1987; **8**(3):171–176.
6. Jakirlic S, Hanjalic K, Tropea C. Modeling rotating and swirling turbulent flows: a perpetual challenge. *AIAA Journal* 2002; **40**(10):1984–1996.
7. Jones WP. Turbulence modelling and numerical solution methods for variable density and combusting flows. In *Turbulent Reacting Flows*, Libby PA, Herausgeber FAW (eds). Chapter 6. Academic Press: London, San Diego, New York, 1994; 309–374.
8. Hogg S, Leschziner MA. Computation of highly swirling confined flow with a Reynolds stress turbulence model. *AIAA Journal* 1989; **27**:57–63.
9. Pascau A. The application of second order turbulence closures to isothermal and combusting swirling flows. *Ph.D. Thesis*, University of London, 1989.
10. Leschziner MA. Turbulence modelling for separated flows with anisotropy-resolving closures. *Philosophical Transactions of the Royal Society of London A* 2000; **358**:3247–3277.
11. Lakehal D, Thiele F. Sensitivity of turbulent shedding flows to non-linear stress-strain relations and Reynolds stress models. *Computers and Fluids* 2001; **30**:1–35.
12. Barakos GN, Drikakis D. Computational study of unsteady turbulent flows around oscillating and ramping aerofoils. *International Journal for Numerical Methods in Fluids* 2003; **42**:163–186.
13. Yang X-D, Ma H-Y. Linear and non-linear eddy-viscosity turbulence models for a confined swirling co-axial jet. *Numerical Heat Transfer, Part B: Fundamentals* 2003; **43**(3):289–305.
14. Yang X-D, Ma H-Y. Computation of strongly swirling confined flows with cubic eddy-viscosity turbulence models. *International Journal for Numerical Methods in Fluids* 2003; **43**:1355–1370.
15. Apsley DD, Leschziner MA. A new low-Re non-linear two-equation turbulence model for complex flows. *International Journal of Heat and Fluid Flow* 1998; **19**:209–222.
16. Merci B, De Langhe C, Vierendeels J, Dick E. A quasi-realizable cubic low-Reynolds eddy-viscosity turbulence model with a new dissipation rate equation. *Flow, Turbulence and Combustion* 2001; **66**:133–157.
17. Launder BE, Sharma BI. Application of the energy-dissipation model of turbulence to the calculation of flow near spinning disc. *Letters in Heat and Mass Transfer* 1974; **1**:131–138.
18. Chassaing P, Antonia RA, Anselmet F, Joly L, Sarkar S. *Variable Density Fluid Turbulence*. Chapter 5. Kluwer Academic Publishers: Dordrecht, 2002.
19. Shih T-H, Lumley JL, Janicka J. Second-order modelling of a variable-density mixing. *Journal of Fluid Mechanics* 1987; **180**:93–116.
20. Favre A. Statistical equations of turbulent gases. In *Problems of Hydrodynamics and Continuum Mechanics*. Society for Industrial and Applied Mathematics, Philadelphia, PA, 1969; 231–266.
21. Ha Minh H, Launder BE, MacInnes J. A new approach to the analysis of turbulent mixing in variable density flows. In *Proceedings of the 3rd Symposium on Turbulent Shear Flows*, Bradbury LJS, Durst F, Launder BE, Schmidt FW, Whitelaw, JH (eds). Davis, CA, September 1981; 19.6.19–19.6.25.
22. Chassaing P, Herard JM. Second order modelling of a variable density turbulent mixing. In *Proceedings of the 6th Symposium on Turbulent Shear Flows*, Launder BE (ed.). Toulouse, France, September 1987; 17.8.1–17.8.6.
23. Chassaing P, Harran G, Joly L. Density fluctuation correlations in free turbulent binary mixing. *Journal of Fluid Mechanics* 1994; **279**:239–278.
24. Sanders JPH, Sarh B, Gokalp I. Variable density effects in axisymmetric isothermal turbulent jets: a comparison between a first- and a second-order turbulence model. *International Journal of Heat and Mass Transfer* 1997; **40**(4):823–842.
25. Chomiak J, Nisbet JR. Modeling variable density effects in turbulent flames: some basic considerations. *Combustion and Flame* 1995; **102**(3):371–386.
26. Merci B, Dick E, Vierendeels J, Roekaerts D, Peeters TWJ. Application of a new cubic turbulence model to piloted and bluff-body diffusion flames. *Combustion and Flame* 2001; **126**:1533–1556.
27. Chassaing P. The modeling of variable density turbulent flows: a review of first-order closure schemes. *Flow, Turbulence and Combustion* 2001; **66**(4):293–332.
28. Chassaing P. Some problems on single point modeling of turbulent, low-speed, variable density fluid motions. In *IUTAM Symposium on Variable Density Low-Speed Turbulent Flows*, Fulachier L, Lumley JL, Anselmet F (eds). Marseille, France. Kluwer Academic Publishers: Netherlands, 1997; 65–84.

29. Speziale CG, Younis BA, Rusinstein R, Zhou Y. On consistency conditions for rotating turbulent flows. *Physics of Fluids* 1998; **10**(8):2108–2110.
30. Bardina J, Ferziger JH, Rogallo R. Effect of rotation on isotropic turbulence: computation and modelling. *Journal of Fluid Mechanics* 1985; **154**:321–336.
31. Jones WP, Pascau A. Calculation of confined swirling flows with a second moment closure. *Journal of Fluids Engineering* 1989; **111**:248–254.
32. Speziale CG, Younis BA, Berger SA. Analysis and modeling of turbulent flow in an axially rotating pipe. *Journal of Fluid Mechanics* 2000; **407**:1–26.
33. Ferziger JH, Perić M. *Computational Methods for Fluid Dynamics*. Chapter 7. Springer: Berlin, 1996.
34. Durst F, Wennerberg D. Numerical aspects of calculation of confined swirling flows with internal recirculation. *International Journal for Numerical Methods in Fluids* 1991; **12**:203–224.
35. Younis BA, Speziale CG, Clark TT. A non-linear algebraic model for the turbulent scalar fluxes. *NASA CR* 201796, 1996.
36. Fulachier L, Borghi R, Anselmet F, Paranthoen P. Influence of density variations on the structure of low-speed turbulent flows: a report on Euromech 237. *Journal of Fluid Mechanics* 1989; **203**:577–593.

